This is the peer-reviewed, final accepted version for American Mineralogist, published by the Mineralogical Society of America.
The published version is subject to change. Cite as Authors (Year) Title. American Mineralogist, in press.
DOI: https://doi.org/10.2138/am-2022-7973. http://www.minsocam.org/

Revision #1

# The crystal structure of $Fe_2S$ at 90 GPa based on single-crystal X-ray diffraction techniques

**Claire C. Zurkowski[a], Barbara Lavina[b,c], Stella Chariton[c], Sergey Tkachev[c], Vitali B. Prakapenka[c], Andrew J. Campbell[a]**

[a]University of Chicago, Department of the Geophysical Sciences, 5734 S Ellis Ave, Chicago, IL 60637, USA

[b]X-ray Science Division, Advanced Photon Source, Argonne National Laboratory, Argonne, IL 60439, USA

[c]Center for Advanced Radiation Sources, University of Chicago, 9700 South Cass Avenue, Building 434A, Argonne, IL 60439, USA

## ABSTRACT

The Fe-S system was explored in a laser-heated diamond-anvil cell at 89(2) GPa and 2380(120) K to better understand the phase stability of $Fe_2S$. Upon temperature quenching, crystallites of $Fe_2S$ were identified and their structure was investigated using single-crystal X-ray diffraction techniques. At these conditions, $Fe_2S$ adopts the *C*23 structure (anti-$PbCl_2$, $Co_2P$) with space group *Pnma* (*Z*=4). This structure consists of columns of corner-sharing, $FeS_4$ tetrahedra and columns of edge-sharing $FeS_5$ square pyramids linked along edges in the *b* direction. Sulfur is in 9-fold coordination with Fe. This study marks the first high-pressure structural solution and refinement of $Fe_2S$ synthesized in a multigrain Fe + FeS sample at 90 GPa

and 2400 K and establishes the stability of *C*23 $Fe_2S$ at these conditions. A previous powder diffraction study reports an orthorhombic $Fe_2S$ phase with a *C*37, $Co_2Si$-like unit cell above 190 GPa. A *C*23–*C*37 structural transition is inferred to explain the previously observed unit-cell parameters at higher pressures and temperatures. These results highlight the utility of applying single-crystal X-ray diffraction techniques to high *P*-*T* multigrain samples to explore the structural properties of iron-rich phases in Earth and planetary cores.

## INTRODUCTION

Equations of state studies of solid and liquid iron reveal that the seismically determined density profile through Earth's core is 3-8% less dense than pure iron (Dewaele et al. 2006; Kuwayama et al. 2020). Cosmochemically abundant light elements such as sulfur, oxygen, silicon, carbon, and hydrogen likely account for this density deficit (e.g. Birch 1952; Jephcoat and Olsen 1987). Exploring the phase stability of Fe-(S, Si, O, C, H) alloys at high pressures and temperatures is therefore critical to constraining core chemistry and thermodynamics. This study focuses on the structural properties of Fe-S alloys as sulfur is likely a significant core-alloying component due to its abundance in iron meteorites thought to originate from planetary cores and its depletion in the silicate Earth compared to chondrites (Scott and Wasson 1975; McDonough and Sun 1995).

Sulfur easily reacts with iron to form numerous high *P*-*T* iron sulfides including FeS, $Fe_3S_2$, $Fe_2S$, and $Fe_3S$ (e.g. Fei et al. 1995; Fei et al. 1997; Fei et al. 2000; Ozawa et al. 2013; Tateno et al. 2019). Experimental studies have reported that tetragonal $Fe_3S$ (*I*-4, *Z*=4) is the stable iron-rich sulfide between 21 and 250 GPa and to high temperatures (Fei et al. 2000; Seagle et al. 2006; Kamada et al. 2010, 2012; Ozawa et al. 2013; Mori et al. 2017; Yokoo et al. 2019),

but *ab-initio* calculations contrarily predict that only FeS and $Fe_2S$ stoichiometries are stable in the 100-400 GPa pressure range (Bazhanova et al. 2017). Experiments at 300 GPa targeting core-relevant compositions have determined that FeS is a low-temperature phase and $Fe_2S$ is a high-temperature phase coexisting with Fe at these conditions (Ozawa et al. 2013; Tateno et al. 2019).

$Fe_2S$ has emerged as a relevant Fe-rich sulfide, particularly in the context of the high *P-T* conditions of Earth's core (Tateno et al. 2019). Two structures have been reported for $Fe_2S$ in the pressure range of 22-306 GPa. TEM analysis of a sample recovered from 22 GPa and 1900 K indicates that $Fe_2S$ assumes the *C*22, $Fe_2P$-type structure at these conditions (Koch-Müller et al. 2002). At high temperatures between 190 and 306 GPa, $Fe_2S$ has been observed to take an orthorhombic lattice (Tateno et al. 2019), with unit-cell parameters compatible with the *C*37 structure ($Co_2Si$ type, *Pnma*, *Z*=4) (Tateno et al. 2019). These results are supported by *ab-initio* calculations predicting a *Pnma* $Fe_2S$ phase to 400 GPa at 300 K (Bazhanova et al. 2017). A recent examination of the analogous $Fe_2P$ system reveals a pressure-induced *C*23-*C*37 transition above 42 GPa (Nakashima et al. 2020), supporting that the *C*37 structure is a high-pressure polymorph in these $Fe_2X$ (*X* = S, P) compounds. Furthermore, as the phase relations observed in the iron phosphide system tend to serve as low pressure analogs to the iron sulfide system (e.g. Rundqvist 1962; Ono et al. 2006; Dera et al. 2008; Gu et al. 2016; Tateno et al. 2019), the *C*23 and *C*37 structures observed in $Fe_2P$ may reflect higher pressure phase relations in $Fe_2S$.

While experimental and calculated results demonstrate that $Fe_2S$ is an important compound to further investigate in relation to Earth's core chemistry, an examination into the crystallography of $Fe_2S$ at high pressures has not been carried out. In the current study, crystallites of $Fe_2S$ were synthesized in a Fe+FeS starting foil in a laser-heated diamond-anvil cell at 90 GPa and 2400 K, and its crystal structure was determined based on single-crystal X-ray

diffraction techniques. Structural solution and refinement of atomic fractional coordinates indicate that the equilibrium phase is a *C*23, $Co_2P$-type $Fe_2S$. These results suggest a *C*23-*C*37 transition in $Fe_2S$ at higher pressures.

## METHODS

The synthesis of $Fe_2S$ was conducted in a laser-heated diamond anvil cell (LHDAC). A starting composition was made mixing Fe (99.9+%, <10 μm, Alfa Aesar) powder with iron sulfide (FeS, 99.99%, Alfa Aesar) powder in a ratio of 1g Fe to 1.75 g FeS in an agate pestle and mortar. The pressure was generated in a BX-90-type (70º angular opening) diamond anvil cell (Kantor et al. 2012) using Type-I conical anvils with 150 μm beveled culets and conical seats. Foils of the starting material were obtained by pressing powders between two ungasketed diamond anvils and then loaded into an 80 μm diameter drilled sample chamber in a rhenium gasket. A ruby ball was then placed near the sample foil and the loaded sample chamber was filled with neon (Rivers et al. 2008). During compression, the ruby fluorescence scale and the Ne equation of state were used to measure pressure (Mao and Bell 1976; Fei et al. 2007). Due to the high compressibility of neon, the sample chamber diameter shrunk to ~15 μm at target pressure.

*In-situ* laser heating and X-ray diffraction experiments took place at beamline 13-ID-D (GeoSoilEnviroCARS) of the Advanced Photon Source, Argonne National Laboratory. The X-ray beam was aligned with the lasers using the fluorescence of the sample (Prakapenka et al. 2008). Samples were then laser-heated from both sides using fiber lasers shaped with ~15 μm flat tops (Prakapenka et al. 2008). Temperature was measured spectroradiometrically based on a gray body approximation fit to the thermal emission from the central 6 μm of the laser-heated spot (Heinz and Jeanloz, 1987). A 3% correction was then applied to account for the thermal

gradient through the sample chamber (Campbell et al. 2007, 2009). Heating cycles typically lasted ~15 minutes at target pressure prior to quenching or until sufficient grain growth was observed. The sample was heated 3 times in different locations of the sample chamber with the goal of maximizing $Fe_2S$ grain growth and data collected after the final heating cycle is reported herein. X-ray diffraction patterns were collected during heating with a beam size of 2 μm x 3 μm beam at 42 keV ( $\lambda$= 0.2952 Å).

Upon quench, a 10 x 10 μm diffraction map was collected in 2 μm steps to determine the regions of the laser-heated area that exhibited the largest grain growth (showing high intensity, spotty XRD) of the target phase. At selected locations, rotation images were collected across a ±30º angular range in 0.5º steps with exposure times of 4 s. Diffraction data were processed using Dioptas (Prescher and Prakapenka 2015) and CrysAlis Pro (Rigaku OD 2018). Quenched multigrain samples consisted of agglomerates of $Fe_2S$ crystallites (up to ~4 μm in diameter) with a few grains of hcp-Fe in more Fe-rich regions of the starting foil. Diffraction rings from the Re were also detected due to the size of the sample chamber at target pressures, but the volumes of Fe and $Fe_2S$ observed do not support Re reaction with the sample. Grains of the target $Fe_2S$ phase were identified in reciprocal space and separated from the reflections attributable to iron, rhenium, neon, and diamond. For each identified $Fe_2S$ lattice, the unit-cell parameters and structure factors were calculated using CrysAlis Pro (Rigaku OD 2018). Structural solution and refinement were conducted using SHELXT (Sheldrick 2015a) and SHELXL2014/7 (Sheldrick 2015b), respectively. Structure solutions were examined during refinement using VESTA (Momma and Izumi 2011). A summarization of the experimental conditions and instrument parameters used in this study are given in the attached CIF file.

This is the peer-reviewed, final accepted version for American Mineralogist, published by the Mineralogical Society of America.
The published version is subject to change. Cite as Authors (Year) Title. American Mineralogist, in press.
DOI: https://doi.org/10.2138/am-2022-7973. http://www.minsocam.org/



# RESULTS AND DISCUSSION

Heating experiments were conducted at 89(2) GPa. Upon quenching from 2380(120) K, several grains, within a 100 $\mu m^2$ region around the laser-heated spot, were identified in the reciprocal space and indexed to an orthorhombic lattice. The grains were found to have similar unit-cell parameters (Table S1), and a selected grain, based on the number of reflections and reduction parameters (Table S2), has the unit-cell lengths: 5.066(2) Å, 3.285(2) Å, and 6.125(2) Å. Analysis of systematic absences constrains a *Pnma* space group and density considerations suggest 4 formula units per cell $Fe_2S$. The orientation matrices of each grain analyzed is provided in Appendix A1.

Despite the limited opening of the DAC and conical seats used to obtain the high *P-T* synthesis conditions; the scattering overlap from diamond, rhenium, and other crystallites in the multigrain sample; and the variation in the volume of the crystal in the path of the beam during the rotational scans, the solution and refinement of all grains at 89 GPa indicate that the synthesized $Fe_2S$ crystallites adopt the *C*23 structure (anti-$PbCl_2$/$Co_2P$-type, *Z*=4) (Rundqvist 1960) (Figure 1). The structural solution and refinement model are robust and repeatable, considering the good agreement of the refined atomic fractional coordinates for each grain (Table S3). After data reduction, 190-260 measured reflections and 82-147 independent reflections were observed for each $Fe_2S$ crystallite, and 0-4 outlying reflections were identified based on anomalous differences in observed versus calculated structure factors and omitted in the final structure calculations (Table S2). Due to the limited reflections collected in these high-pressure measurements, not all sites could be refined with anisotropic displacement parameters (Table S3). Instead, when sufficient reflections were observed, the Fe sites were refined with anisotropic displacement parameters while the S site was refined with isotropic displacement

parameters (Table S3). Otherwise, all sites were refined with isotropic displacement parameters (Table S3). Within 1%, all sites for all grains are fully occupied. A CIF file of the refined solution model is provided in Supplementary Material. The uniformity of unit-cell parameters and site occupancies suggest invariable stoichiometry and structure from grain to grain.

The *C*23 $Fe_2S$ structure can be viewed as corner-sharing columns of $FeS_4$ tetrahedra and columns of edge-sharing $FeS_5$ square pyramids linked along edges in the *b* direction (Figure 1a). The Fe1, Fe2, and S3 sites occupy Wyckoff position 4*c* with point symmetry *m* (Table S3). Sulfur is coordinated by 9 iron atoms (Figure 1b, Table 1). The Fe1, Fe2, and S coordination environments observed differentiate this structure from the *C*37, $Co_2Si$-type structure. $M_2X$ compounds in the *C*37 structure have the same space group and site symmetries as compounds with the *C*23 structure, but *C*37 phases have one 10-fold coordinated *X* site and two 5-fold coordinated *M* sites (Geller and Wollontis 1955; Rundqvist 1960; Hyde et al. 1992) while *C*23 phases have one 9-fold coordinated *X* site, one 4-fold coordinated *M* site, and one 5-fold coordinated *M* site. S–Fe interatomic distances in *C*23 $Fe_2S$ range from 1.994(2) Å to 2.357(1) with the tenth closest Fe atom at 3.077(3) Å, suppoting 9-fold coordination of Fe around the S sites. Fe–S distances in the $FeS_4$ tetrahedra range from 2.110(2) Å to 2.359(1) Å with the next nearest S atom at 3.063(3) Å, supporting 4-fold coordinated Fe site. The interatomic distances measured in $Fe_2S$ at 89(2) GPa are given in Table 1. These bond lengths are comparable to those measured in $Fe_3S$, FeS, and $FeS_2$ (Brostigen and Kjekshus 1969; Lennie et al. 1995; Fei et al. 2000) considering the degree of compression of the Fe-S bond at 89 GPa.

The integration of the diffraction patterns collected in each rotational scan shows the presence of *C*23 $Fe_2S$ crystallites, and Re and Ne (Figure 2). Unit-cell volumes and site occupancies of the $Fe_2S$ grains analyzed (Table S3), verify that Re did not react into the sample.

Rhenium diffraction, likely from the gasket-hole edge, is an outcome of the small hole size at these high pressures. $Fe_2S$ in the raw diffraction patterns appears as spotty Debye rings, showing a range of grain sizes formed at the synthesis conditions (Figure 2, red tick marks). In the integrated patterns, $Fe_2S$ accounts for nearly all of the lower-intensity peaks, compared to Ne and Re (Figure 2). An additional peak at around $2\Theta \sim 9.1^{o}$ remains unidentified (Figure 2), but it appears as a weak powder ring in the raw patterns, indicating that it is not diffraction from the synthesized *C*23 $Fe_2S$ crystallites. In Figure 2b and 2c, a few additional reflections are marked as unidentified. No additional lattice-types were identified in the reciprocal space, indicating that these unidentified diffraction spots are not associated with *C*23 $Fe_2S$ and are not a part of a well-formed crystal lattice in the sample chamber. The calculated diffraction lines for *C*23 $Fe_2S$ based on the single-crystal analyses are shown in red below the integrated diffraction pattern in Figure 2 and higher intensity miller indices are labeled. The calculated *hkl* values, d-spacings, $2\Theta$ values, and Q values are provided in Appendix A2.

At the sample locations where grains 3-6 were identified (Table S1), crystallites of Fe are also observed, indicating a more iron-rich region of the starting material. In the cases where Fe is present in the diffraction patterns, it is observed in the hcp-phase and identified based on diffraction from the (100), (002), (101), (102), (110), (112), and (201) planes. Sharp, high-intensity spots overlain on faint rings at the hcp-Fe diffraction angles indicate recrystallized iron coexisting with $Fe_2S$ (Figure S1). At other locations, such as the locations where grains 1 and 2 were identified (Table S1), all of the initial Fe has reacted with FeS to form $Fe_2S$, such that no diffraction from hcp-Fe are observed (Figure 2). If these sample locations where hcp-Fe is not observed are associated with more S-rich regions of the starting material, than the additional unidentified reflections (Figure 2b, c) may indicate the presence of a coexisting sulfide that is

more S-rich than $Fe_2S$. Further experiments, aimed at assessing the equilibrium phase relations is required to explain these observations.

$Fe_2S$ has previously been reported to take an orthorhombic structure in the pressure range of 190-306 GPa and up to 3600 K with unit-cell parameters compatible with the *C*37 structure (Tateno et al. 2019). This *C*37 $Fe_2S$ structure was proposed without verification from single-crystal techniques, but insight can be gained from the systematic comparison of the $Co_2P$ and $Co_2Si$ unit cells, which can serve as analogs of the $Fe_2S$ polymorphs. At ambient conditions, *C*23 $Co_2P$ has a longer *a* axis and shorter *b* and *c* axis than that of *C*37 $Co_2Si$ (Rundqvist 1960), and $Co_2P$ has a *c/a* ratio of 1.16 while $Co_2Si$ has a *c/a* ratio of 1.44 (Rundqvist 1960; Geller and Walantis 1955). Between 190 and 300 GPa, Tateno et al. (2019) report $Fe_2S$ *c/a* ratios in the 1.35-1.40 range, and at 90 GPa, the current study reports a $Fe_2S$ *c/a* ratio of 1.21. These relative unit-cell analyses support that the *C*37 $Fe_2S$ is the stable phase at higher pressures (Tateno et al. 2019), while the structural solution and refinement carried out in this study establishes that $Fe_2S$ adopts the *C*23 structure at 90 GPa.

## IMPLICATIONS

Upon pressurization to 90 GPa and heating to 2400 K, $Fe_2S$ was synthesized and its structure was determined using single-crystal X-ray diffraction techniques on a multigrain Fe+FeS starting material. Structural solution and refinement of 6 crystallites prove that $Fe_2S$ takes a *C*23 structure (*Pnma, Z*=4) at these conditions. While Earth's core-mantle boundary (CMB) pressure is 136 GPa, exceeding the pressure conditions of the current study, broad understanding of stable iron sulfide phases is important to assess the behavior of Fe,S-rich systems relevant to Earth's core. Moreover, the C23 $Fe_2S$ phase may be important in the

crystallization sequences within smaller terrestrial planets. Future experiments at lower pressures, may elucidate the stability of $Fe_2S$ versus $Fe_3S$ and $Fe_3S_2$ at conditions related to the Martian and Mercurian core. A recent multi-anvil press study revealed that Si may expand the stability field of $Fe_2S$ at the conditions of the Mercurian inner core boundary (ICB), but no structure information was obtained for this $Fe_2(S, Si)$ phase (Tao et al. 2021).

In relationship to Earth's core, $Fe_2S$ has been observed at Earth's mid-outer-core pressures (190-306 GPa) to have a unit-cell with geometry compatible with a *C*37 structure (Tateno et al. 2019). Analogous to the $Fe_2P$ system (Nakajima et al. 2020), $Fe_2S$ may therefore undergo a *C*23–*C*37 transition within the 89–190 GPa range. Future crystallographic work, tracking the coordination of $Fe_2S$ within this pressure range is needed to determine the *C*23 and *C*37 *P-T* stability fields. This analysis would reveal the structure of $Fe_2S$ at Earth's CMB pressures and high temperatures and help characterize the density profile of $Fe_2S$ throughout the conditions of the outer core (136-330 GPa, ~4000-6000 K). As both *C*23 $Fe_2S$ and *C*37 $Fe_2S$ take the space group *Pnma* with *Z*=4, the results from this work and that of Tateno et al., 2019 remain in agreement with *ab-initio* calculations on $Fe_2S$ (Bazhanova et al., 2017) and set a framework for future structural exploration of $Fe_2S$.

To further underscore the importance of investigating $Fe_2S$ at conditions relevant to Earth's core, this work demonstrates the co-crystallization of hcp-Fe with *C*23 $Fe_2S$ at 90 GPa and 2400 K (Figure S1). *C*23 $Fe_2S$ is, therefore, the stable sulfide in Fe-rich compositions at these *P-T* conditions, in contrast to previous interpretations of $Fe_2S$ coexisting with Fe at high temperatures only above 250 GPa (Ozawa et al., 2013; Tateno et al. 2019). While the focus of this study was not on the Fe-S phase relations, observations of $Fe_2S$ and Fe crystallizing at high

pressures and temperatures necessitates consideration of $Fe_2S$ in the Fe-rich thermodynamics occurring in Earth's core.

This work marks the first characterization of the lattice geometry and atomic fractional coordinates of $Fe_2S$ based on data collected at high pressures and quenched from high temperatures. Synthesis of $Fe_2S$ with increasing pressure and temperature will provide key insight into the material properties of Fe-rich sulfides in Earth's core and, based on the current results, single-crystal X-ray diffraction is an effective technique for probing the iron-sulfide phases that stabilize at these extreme conditions.

## ACKNOWLEDGEMENTS

Portions of this work were performed at GeoSoilEnviroCARS (The University of Chicago, Sector 13), Advanced Photon Source (APS), Argonne National Laboratory. GeoSoilEnviroCARS is supported by the National Science Foundation - Earth Sciences (EAR - 1634415) and Department of Energy- GeoSciences (DE-FG02-94ER14466). This research used resources of the Advanced Photon Source, a U.S. Department of Energy (DOE) Office of Science User Facility operated for the DOE Office of Science by Argonne National Laboratory under Contract No. DE-AC02-06CH11357. This material is based upon work supported by a National Science Foundation Graduate Research Fellowship to C.C.Z. This work was also supported by the National Science Foundation by grant EAR-1651017 to A.J.C.

## REFERENCES

Baur, W.H. (1974) The geometry of polyhedral distortions. Predictive relationships for the

phosphate group. Acta Crystallographica Section B: Structural Crystallography and Crystal Chemistry, 30, 1195–1215.

Bazhanova, Z.G., Roizen, V.V., and Oganov, A.R. (2017) High-pressure behavior of the Fe-S system and composition of the Earth's inner core. Uspekhi Fizicheskih Nauk, 187, 1105–1113

Birch, F. (1952) Elasticity and constitution of the Earth's interior. Journal of Geophysical Research, 57, 227–286.

Brostigen, G. and Kjekshus, A. (1969) Redetermined crystal structure of $FeS_2$ (Pyrite). Acta Chemica Scandinavica, 23, 2186–2188.

Campbell, A.J., Seagle, C.T., Heinz, D. L., Shen, G., and Prakapenka, V.B. (2007) Partial melting in the iron-sulfur system at high pressure: A synchrotron X-ray diffraction study. Physics of the Earth and Planetary Interiors, 162, 119–128.

Campbell, A.J., Danielson, L., Righter, K., Seagle, C.T., Wang, Y. and Prakapenka, V.B. (2009) High pressure effects on the iron–iron oxide and nickel–nickel oxide oxygen fugacity buffers. Earth and Planetary Science Letters, 286, 556–564.

Dewaele, A., Loubeyre, P., Occelli, F., Mezouar, M., Dorogokupets, P.I. and Torrent, M. (2006) Quasihydrostatic equation of state of iron above 2 Mbar. Physical Review Letters, 97, 215504.

Fei, Y., Prewitt, C.T., Mao, H.K. and Bertka, C.M. (1995). Structure and density of FeS at high pressure and high temperature and the internal structure of Mars. Science, 268, 1892–1894.

Fei, Y., Bertka, C.M. and Finger, L.W. (1997) High-pressure iron-sulfur compound, $Fe_3S_2$, and melting relations in the Fe–FeS system. Science, 275, 1621–1623.

Fei, Y., Li, J., Bertka, C.M. and Prewitt, C.T. (2000) Structure type and bulk modulus of $Fe_3S$, a new iron-sulfur compound. American Mineralogist, 85, 1830–1833.

Fei, Y., Ricolleau, A., Frank, M., Mibe, K., Shen, G. and Prakapenka, V. (2007) Toward an internally consistent pressure scale. Proceedings of the National Academy of Sciences, 104, 9182–9186.

Geller, S., and Wolontis, V.M. (1955) The crystal structure of Co2Si. Acta Crystallographica, 8, 83–87.

Gu, T., Fei, Y., Wu, X. and Qin, S. (2016) Phase stabilities and spin transitions of $Fe_3(S_{1-x}P_x)$ at high pressure and its implications in meteorites. American Mineralogist, 101, 205–210.

Heinz, D.L., and Jeanloz, R. (1987) Measurement of the melting curve of $Mg_{0.9}Fe_{0.1}SiO_3$ at lower mantle conditions and its geophysical implications. Journal of Geophysical Research, 92, 437–444.

Hyde, B.G., O'Keeffe, M., Lyttle, W.M. and Brese, N.E. (1992) Alternative descriptions of the *C*23 ($PbCl_2$), C37 ($Co_2Si$), $B8_b$ ($Ni_2In$) and related structure types. Acta chemica scandinavica (Copenhagen. 1989*)*, 46, 216–223.

Jephcoat, A. and Olson, P., (1987) Is the inner core of the Earth pure iron? Nature, 325, 332–335.

Kamada, S., Terasaki, H., Ohtani, E., Sakai, T., Kikegawa, T., Ohishi, Y., Hirao, N., Sata, N. and Kondo, T. (2010) Phase relationships of the Fe–FeS system in conditions up to the Earth's outer core. Earth and Planetary Science Letters, 294, 94–100.

Kantor, I., Prakapenka, V., Kantor, A., Dera, P., Kurnosov, A., Sinogeikin, S., Dubrovinskaia, N. and Dubrovinsky, L. (2012) BX90: A new diamond anvil cell design for X-ray diffraction and optical measurements. Review of Scientific Instruments, 83, 125102.

298 Koch-Müller, M., Fei, Y., Wirth, R. and Bertka, C.M. (2002) Characterization of high-pressure
299 iron-sulfur compounds. LPI, 1424.
300 Kuwayama, Y., Morard, G., Nakajima, Y., Hirose, K., Baron, A.Q.R., Kawaguchi, S.I.,
301 Tsuchiya,
302 T., Ishikawa, D., Hirao, N., and Ohishi, Y. (2020) Equation of state of liquid iron under
303 extreme conditions. Physical Review Letters, 124, 165701.
304 Lennie, A.R., Redfern, S.A., Schofield, P.F. and Vaughan, D.J. (1995). Synthesis and Rietveld
305 crystal structure refinement of mackinawite, tetragonal FeS. Mineralogical Magazine, 59,
306 677–683.
307 Mao, H.K. and Bell, P.M. (1976) High-pressure physics: the 1-megabar mark on the ruby R1
308 static pressure scale. Science, 19, 851–852.
309 McDonough, W.F. and Sun, S.S. (1995) The composition of the Earth. Chemical geology, 120,
310 223–253.
311 Momma, K. and Izumi, F. (2011). VESTA 3 for three-dimensional visualization of crystal,
312 volumetric and morphology data. Journal of applied crystallography, 44, 1272–1276.
313 Mori, Y., Ozawa, H., Hirose, K., Sinmyo, R., Tateno, S., Morard, G. and Ohishi, Y. (2017)
314 Melting experiments on Fe–$Fe_3S$ system to 254 GPa. Earth and Planetary Science Letters,
315 464 135–141.
316 Nakajima, Y., Araki, S., Kinoshita, D., Hirose, K., Tateno, S., Kawaguchi, S.I. and Hirao, N.
317 (2020) New pressure-induced phase transition to $Co_2Si$-type $Fe_2P$. American
318 Mineralogist, 105, 1752–1755.
319 Ono, S. and Kikegawa, T. (2006) High-pressure study of FeS, between 20 and 120 GPa, using
320 synchrotron X-ray powder diffraction. American Mineralogist, 91, 1941–1944.

Ozawa, H., Hirose, K., Suzuki, T., Ohishi, Y. and Hirao, N. (2013) Decomposition of $Fe_3S$ above 250 GPa. Geophysical research letters, 40, 4845–4849.

Prakapenka, V.B., Kubo, A., Kuznetsov, A.Laskin, A., Shkurikhin, O., Dera, P., Rivers, M. L. and Sutton, S.R. (2008) Advanced flat top laser heating system for high pressure research at GSECARS: application to the melting behavior of germanium. High Pressure Research, 28, 225–235.

Prescher, C., and Prakapenka, V.B. (2015) DIOPTAS: a program for reduction of two dimensional X-ray diffraction and data exploration. High Pressure Research, 35(3), 223–230.

Rigaku Oxford Diffraction (2018) CrysAlisPRO software system, ver. 1.171.39.44a Rigaku Corporation, Oxford, U.K

Rundqvist, S. (1960) The structures of $Co_2P$, $Ru_2P$ and related phases. Acta Chemica. Scandinavica, 14, 1961–1979.

Rundqvist, S. (1962) Phosphides of the B31 (MnP) structure type. Acta Chemica Scandinavica 16, 287–292.

Tao, R. and Fei, Y. (2021) High-pressure experimental constraints of partitioning behavior of Si and S at the Mercury's inner core boundary. Earth and Planetary Science Letters 562, 116849.

Tateno, S., Ozawa, H., Hirose, K., Suzuki, T., I-Kawaguchi, S., and Hirao, N. (2019) $Fe_2S$: the most Fe-rich iron sulfide at the Earth’s inner core pressures. Geophysical Research Letters, 46, 11,944–11,949.

Scott, E.R. and Wasson, J.T. (1975) Classification and properties of iron meteorites. Reviews of Geophysics, 13, 527–546.

344 Seagle, C.T., Campbell, A.J., Heinz, D.L., Shen, G. and Prakapenka, V.B. (2006) Thermal
345 equation of state of $Fe_3S$ and implications for sulfur in Earth's core. Journal of
346 Geophysical Research: Solid Earth, 111.
347 Sheldrick, G.M. (2015a) SHELXT–Integrated space-group and crystal-structure determination.
348 Acta Crystallographica Section A: Foundations and Advances, 71, 3–8.
349 Sheldrick, G.M. (2015b) Crystal structure refinement with SHELXL. Acta Crystallographica
350 Section C: Structural Chemistry, 71, 3–8.
351 Yokoo, S., Hirose, K., Sinmyo, R. and Tagawa, S. (2019) Melting Experiments on Liquidus
352 Phase Relations in the Fe-S-O Ternary System Under Core Pressures. Geophysical
353 Research Letters, 46, 5137–5145.
354
355
356
357
358
359
360
361
362
363
364
365
366

# FIGURE CAPTIONS

**Figure 1.** *C*23 $Fe_2S$, synthesized at 89(2) GPa and 2380(112) K with iron atoms in dark blue and sulfur atoms in light pink. a) Polyhedral view of $Fe_2S$ showing Fe-coordination polyhedra. In this view, the unit cell is composed of $FeS_4$ tetrahedra and $FeS_5$ square pyramids in a 1:1 ratio. The tetrahedral and square pyramid building blocks are shown on the right. b) Polyhedral view of $Fe_2S$ showing S-coordination polyhedra. In this view, the unit cell is composed of $SFe_9$ polyhedra. The $SFe_9$ building block is shown on the right.

**Figure 2. a)** Raw X-ray diffraction pattern at 89(2) GPa produced by combining the images collected across ±30º rotation in 0.5º steps with 4 s exposure per image. **b)** Zoomed-in portion of the raw diffraction images. Red tick marks indicate the diffraction angles of *C*23 $Fe_2S$ and the respective Miller Indices labeled. Diffraction angles associated with neon (blue) and rhenium (green) are also labeled and rings or spots that were not indexed to these phases are labeled with a question mark (?). The high intensity spot, labeled with a "C," is a diamond reflection. **c)** Integrated X-ray diffraction pattern with the calculated d-spacings based on the *C*23 $Fe_2S$ analyses shown as the red tick marks below the pattern. Selected higher intensity $Fe_2S$ peaks are labeled with their corresponding Miller indices. Peaks associated with Re and Ne are labeled in green and blue respectively. Unknown peaks are labeled with a question mark. Scattering from diamond has been masked out of the integrated pattern. The Miller indices, intensities, d-spacings, 2Θ values and Q values calculated for *C*23 $Fe_2S$ are given in Appendix A2.

# TABLES

**Table 1.** Interatomic distances, polyhedra volumes and distortion indices (Baur, 1974) measured in the coordination polyhedra of *C*23 $Fe_2S$ at 89(2) GPa.

| Polyhedron | Sites | Interatomic Distance (Å) | Polyhedra Volume (Å$^3$) | Distortion Index |
|---|---|---|---|---|
| **$FeS_5$** | | | 8.462 | 0.042 |
| | **Fe1–S3** | 2.110(2) | | |
| | **Fe1–S3** | 2.190(1) | | |
| | **Fe1–S3** | 2.190(1) | | |
| | **Fe1–S3** | 2.359(1) | | |
| | **Fe1–S3** | 2.359(1) | | |
| **$FeS_5$** | | | 4.263 | 0.012 |
| | **Fe2–S3** | 1.994(2) | | |
| | **Fe2–S3** | 2.047(2) | | |
| | **Fe2–S3** | 2.066(1) | | |
| | **Fe2–S3** | 2.066(1) | | |
| **$SFe_9$** | | | 20.016 | 0.050 |
| | **S3–Fe2** | 1.994(2) | | |
| | **S3–Fe2** | 2.047(2) | | |
| | **S3–Fe2** | 2.066(1) | | |
| | **S3–Fe2** | 2.066(1) | | |
| | **S3–Fe1** | 2.110(2) | | |
| | **S3–Fe1** | 2.190(1) | | |
| | **S3–Fe1** | 2.190(1) | | |
| | **S3–Fe1** | 2.359(1) | | |
| | **S3–Fe1** | 2.359(1) | | |

This is the peer-reviewed, final accepted version for American Mineralogist, published by the Mineralogical Society of America.
The published version is subject to change. Cite as Authors (Year) Title. American Mineralogist, in press.
DOI: https://doi.org/10.2138/am-2022-7973. http://www.minsocam.org/

Revision #1

401

402

403

404 # FIGURES

405 **Figure 1.**

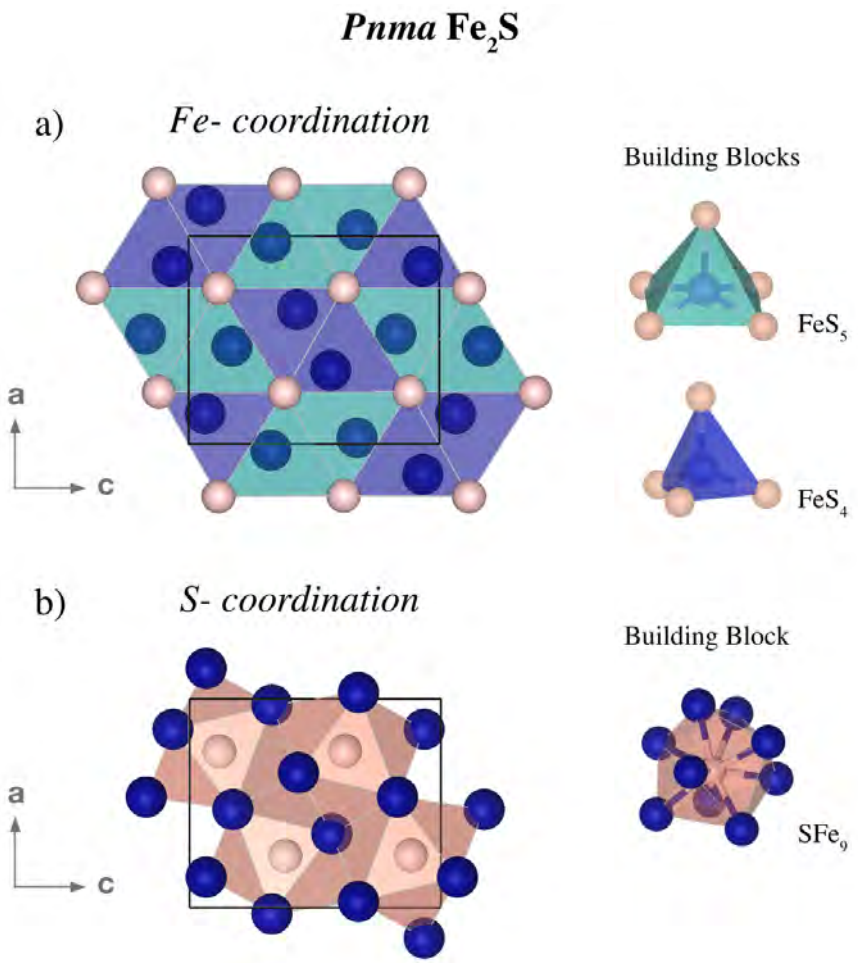


406

407

408

409

410

411

412

413

414

415

416

417

This is the peer-reviewed, final accepted version for American Mineralogist, published by the Mineralogical Society of America.
The published version is subject to change. Cite as Authors (Year) Title. American Mineralogist, in press.
DOI: https://doi.org/10.2138/am-2022-7973. http://www.minsocam.org/

Revision #1

**Figure 2.**

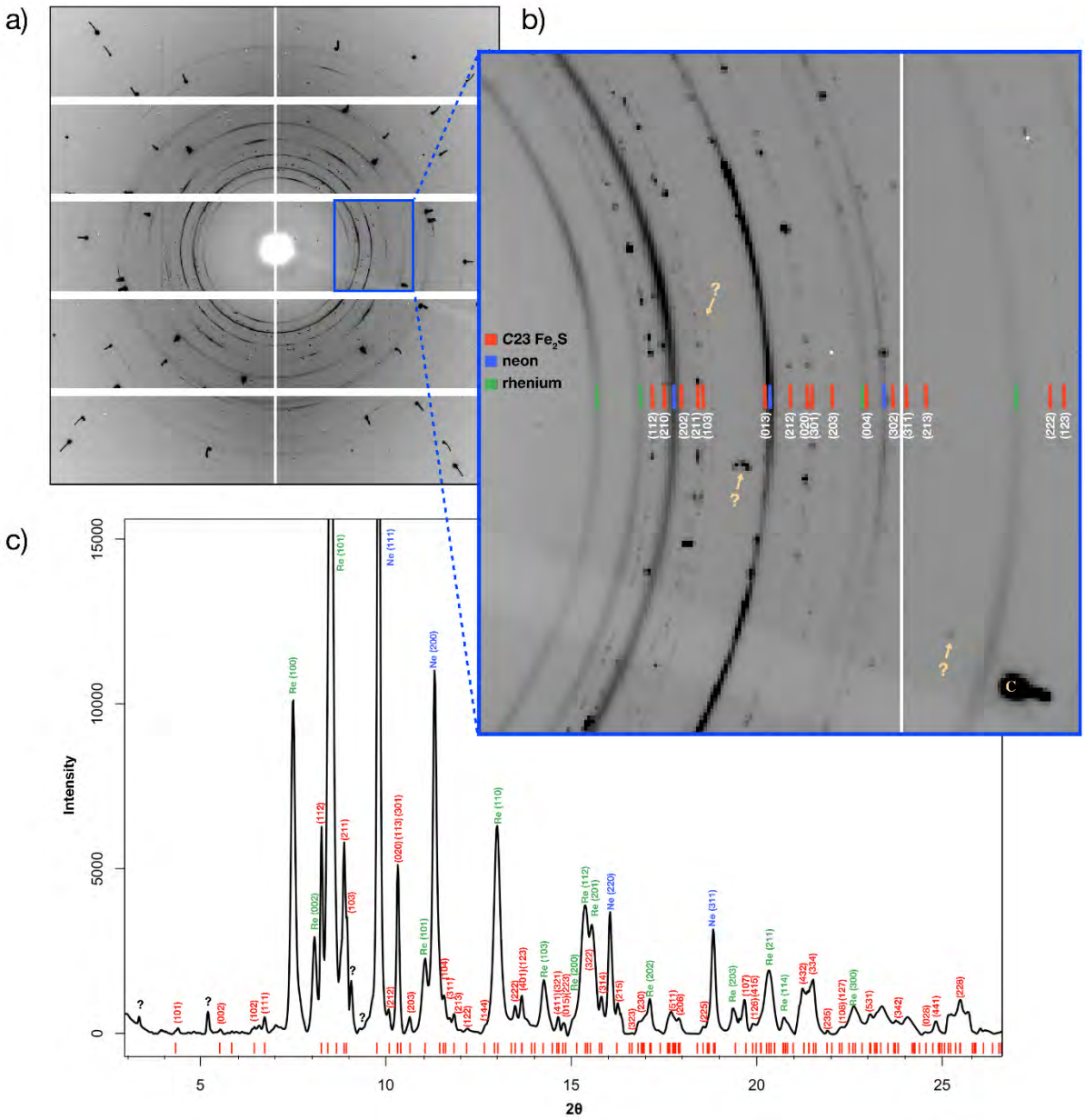

This is the peer-reviewed, final accepted version for American Mineralogist, published by the Mineralogical Society of America.
The published version is subject to change. Cite as Authors (Year) Title. American Mineralogist, in press.
DOI: https://doi.org/10.2138/am-2022-7973. http://www.minsocam.org/

**Figure 1**

# Figure 2